SAR IMAGE RECONSTRUCTION FOR AN ARBITRARY RADAR PATH

Jennifer L.H. Webb and David C. Munson, Jr.

Coordinated Science Laboratory and
Department of Electrical and Computer Engineering
University of Illinois at Urbana-Champaign
1308 West Main Street, Urbana, IL 61801

ABSTRACT

We consider the problem of spotlight-mode synthetic aperture radar (SAR) imaging for an arbitrary radar path. A general imaging scenario involves a 3-D scattering surface with data collected along an arbitrary 3-D radar path. This approach is useful, for example, in military applications where the radar platform may undergo some maneuvers, and in radar astronomy where the relative motion is, at least in part, determined by the natural paths of celestial bodies. We show that nonideal platform motion can create phase variations in the data which lead to spatially-varying shifts and blurring. A correction procedure is proposed and demonstrated.

1. BACKGROUND

We consider the problem of SAR imaging for an arbitrary radar path. Most SAR formulations assume an ideal radar path, such as from rectilinear motion. However, there are cases where the radar platform may be required to follow some other path, such as in military applications or in radar astronomy. For instance, we have processed Lunar data from Arecibo Observatory, where the relative motion is determined by the rotation and orbit of the Earth and Moon [1]. We have seen that even slight deviation from the ideal radar path causes degradation in Lunar images formed with a 2-D SAR algorithm.

In principle, data from a 3-D radar path can be used to form a 3-D image, using an extension of the 2-D polar-format spotlight-mode SAR algorithm [2, 3, 4]. Any given range-bin datum is a measure of the projection of the reflectivity of all illuminated scatterers lying along an approximately planar wavefront; the 1-D Fourier Transform (FT) of a set of planar projections yields a linear ray of the 3-D FT, according to a 3-D extension of the projection-slice theorem. Thus, 3-D Fourier samples are computed via an FFT of the range-bin data, and the 3-D Fourier data can be inverse transformed to form a 3-D image. However, in practice, what is often most useful is a 2-D image formed by projecting the 3-D surface onto a plane.

If the shape of the scattering surface is known *a priori* (e.g. a sphere), it is possible to form a sparse 3-D image from sparse 3-D Fourier data. In principle, this can be done by solving a set of simultaneous equations of the form

$$F(X_i, Y_i, Z_i) = \sum_k f(x_k, y_k, z_k) e^{-j(x_k X_i + y_k Y_i + z_k Z_i)} \quad (1)$$

where (x_k, y_k, z_k) is a spatial location on the known scattering surface, $F(\cdot,\cdot,\cdot)$ are the measured Fourier samples and $f(\cdot,\cdot,\cdot)$ are unknown reflectivities, which can be mapped onto a 2-D image. However, for a $M \times N$ image, solution requires inversion of a $NM \times NM$ matrix, with computational complexity $O(N^3M^3)$. Moreover, the matrix may be ill-conditioned. Thus, this method is generally impractical, unless the form of the set of equations is such that well conditioned, fast methods, such as an FFT, can be used.

The approach taken here is to modify the 2-D imaging algorithm based on a 3-D analysis of the effect of variations in the radar path. Section 2 shows that a nonideal radar path results in a multiplicative phase error in the Fourier domain. In Section 3, we linearize the phase error, and derive the corresponding shifts in the spatial domain. Section 4 presents a method for compensating for linear phase error, along with some examples. The resulting method is relatively efficient, numerically well conditioned, and though not exact, effectively compensates for the Fourier phase error associated with an arbitrary path.

2. DERIVATION FOR AN ARBITRARY RADAR PATH

Suppose the radar transmits a nominal pulse of the form

$$s(t) = e^{j\omega_o t}; \qquad 0 \le t \le T, \quad (2)$$

where T is the *compressed* pulse width and ω_o is the radar center frequency. Note that some form of range compression may have been used to achieve the range resolution of the nominal waveform. The return from the n^{th} pulse at time t after start of transmission is

$$p_n(t) = A \cdot \int_{\frac{c(t-T)}{2} \le r_n(x,y,z) \le \frac{ct}{2}} dx \int dy \int dz \quad f(x,y,z) e^{j\omega_o (t - \frac{2}{c} r_n(x,y,z))} \quad (3)$$

where $f(x,y,z)$ is the complex reflectivity, $r_n(x,y,z)$ is the range between the radar and (x,y,z) at the time of the n^{th} pulse, and A is a scale factor accounting for transmit power, attenuation factors, etc. The demodulated return for range bin k, $\bar{p}_n(k)$, is phase corrected to remove the motion of the

This work was supported by the Joint Services Electronics Program under contracts DAAL03-92-G-0139 and N00014-90-J1270.

0-7803-2431-5/95 $4.00

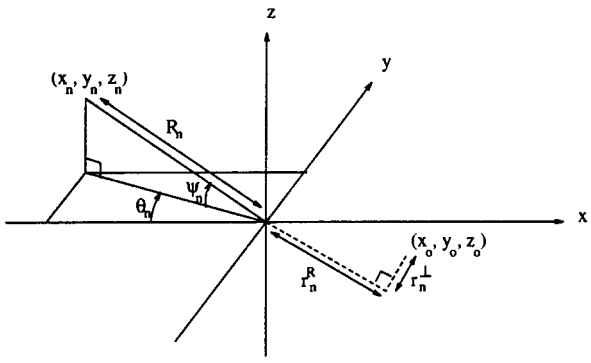

Figure 1: Imaging geometry for radar at (x_n, y_n, z_n).

center point, and thereby simulate constant distance from the center of the imaging area, i.e. $r(0,0,0) \equiv 0$:

$$\bar{p}_n(k) = A \cdot \int_{kT+\frac{2}{c}R_n}^{(k+1)T+\frac{2}{c}R_n} dt \;\; e^{-j\omega_o t} p_n(t) e^{j\omega_o \frac{2}{c}R_n} \qquad (4)$$

for $k = -\frac{K}{2}+1, \ldots, \frac{K}{2}$. By proper choice of units, and assuming constant attenuation over time, we can treat the product of all scale factors as unity. Then the range-bin value is approximately

$$\bar{p}_n(k) \approx \int_{r_n(x,y,z)-R_n \approx \frac{ckT}{2}} dx \int dy \int dz \; f(x,y,z) e^{-j\frac{2\omega_o}{c}(r_n(x,y,z)-R_n)}. \qquad (5)$$

Consider a single point scatterer

$$f(x,y,z) = \delta(x-x_o, y-y_o, z-z_o), \qquad (6)$$

where most of the range-bin values will be zero. Ignoring the possibility of range-bin straddling, the nonempty range bin occurs for $r_n(x_o,y_o,z_o) - R_n \approx \frac{ckT}{2} = k\delta_R$, where δ_R is the range resolution, i.e.

$$\bar{p}_n(k) = \begin{cases} e^{-j\frac{2\omega_o}{c}(r_n(x_o,y_o,z_o)-R_n)} & k = \frac{r_n(x_o,y_o,z_o)-R_n}{\delta_R} \\ 0 & \text{otherwise.} \end{cases} \qquad (7)$$

The range to a given point scatterer depends on the position of the radar, which can be described in spherical coordinates (R_n, θ_n, ψ_n), given relative to the center of the imaging area, as shown in Figure 1. The corresponding Cartesian coordinates are

$$\begin{aligned} x_n &= -R_n cos\theta_n cos\psi_n \\ y_n &= R_n sin\theta_n cos\psi_n \\ z_n &= R_n sin\psi_n. \end{aligned} \qquad (8)$$

The orientation of the axes is such that the radar travels nominally in the x-y plane with viewing angle θ near zero. We seek to form the 2-D image $\hat{f}(x,y) = \int dz\, f(x,y,z)$. For the usual case where the illuminated scatterers are concentrated on a surface that can be described as a function of x and y, the integral merely results in a top view of the surface reflectivity. A Taylor series expansion of

$$r_n(x,y,z) = \sqrt{(x_n-x)^2 + (y_n-y)^2 + (z_n-z)^2} \qquad (9)$$

yields

$$r_n(x,y,z) \approx R_n + r_n^R(x,y,z) + \frac{(r_n^\perp(x,y,z))^2}{2R_n} \qquad (10)$$

where

$$r_n^R(x,y,z) = xcos\theta_n cos\psi_n - ysin\theta_n cos\psi_n - zsin\psi_n \qquad (11)$$

and

$$r_n^\perp(x,y,z) = \sqrt{(x^2+y^2+z^2) - r_n^R(x,y,z)^2}. \qquad (12)$$

The term r_n^R gives the displacement from the origin in the "range" direction (from the radar to the origin), while $r_n^\perp(x_o,y_o,z_o)$ is the orthogonal component of the displacement. For relatively large R_n, the last term is small in (10). Note that without the last term, the range approximation would correspond to a planar wavefront assumption.

Return now to the point-scatterer range-bin data, where the arguments of $r_n(\cdot,\cdot,\cdot)$ and $r_n^\perp(\cdot,\cdot,\cdot)$ will be omitted for simplicity. Even though we cannot apply the 2-D projection-slice theorem, an FFT of the range-bin data still yields information about the 2-D FFT of $f(x,y) = \delta(x-x_o, y-y_o)$. Specifically, for K range bins, the FFT of $\bar{p}$ is

$$\begin{aligned} \bar{P}_n(m) &= \sum_{k=-K/2+1}^{K/2} \bar{p}_n(k) e^{-j\frac{2\pi}{K}km} \\ &= e^{-j(r_n-R_n)(\frac{2\omega_o}{c}+\frac{2\pi}{K\delta_R}m)} \\ &= e^{-j(r_n-R_n)\Omega_m} \\ &= e^{-j(x_o cos\theta_n cos\psi_n - y_o sin\theta_n cos\psi_n)\Omega_m} e^{-j\bar{\phi}_e(n,m)} \\ &= \hat{F}(X_{n,m}, Y_{n,m}) e^{-j\bar{\phi}_e(n,m)} \end{aligned} \qquad (13)$$

where

$$\begin{aligned} \bar{\phi}_e(n,m) &= z_o Z_{n.m} + \frac{\Omega_m}{2R_n}[r_n^\perp]^2 \qquad (14) \\ \Omega_m &= \frac{2\omega_o}{c} + \frac{2\pi}{K\delta_R}m \qquad m = -\frac{K}{2}+1, \ldots, \frac{K}{2} \\ X_{n,m} &= \Omega_m cos\theta_n cos\psi_n \\ Y_{n,m} &= -\Omega_m sin\theta_n cos\psi_n \\ Z_{n,m} &= -\Omega_m sin\psi_n. \end{aligned}$$

Thus, the effect of wavefront curvature and a nonideal radar path can be modeled as a phase error in the Fourier domain. Instead of computing samples of the Fourier data, as would be the ideal case with a planar wavefront and radar path in the x-y plane, the data computed are corrupted with a multiplicative phase error $e^{-j\bar{\phi}_e}$.

3. IMPACT ON IMAGING

Over sufficiently small regions of the Fourier data, the phase error can be approximated with

$$\begin{aligned} \phi_e(X,Y) \approx \phi_e|_{(X_o,Y_o)} &+ \frac{\partial\phi_e}{\partial X}|_{(X_o,Y_o)}(X-X_o) \\ &+ \frac{\partial\phi_e}{\partial Y}|_{(X_o,Y_o)}(Y-Y_o) \end{aligned} \qquad (15)$$

where (X_o, Y_o) is the center of the Fourier data, and ϕ_e is a continuous function such that $\bar{\phi}_e(n,m) = \phi_e(X_{n,m}, Y_{n,m})$.

The linear phase modulation will result in a shift in the spatial data, which is spatially-varying, since ϕ_e depends on the location (x_o, y_o, z_o) of the point scatterer.

The amount of shift is the value of the corresponding partial derivative evaluated at the center of the Fourier data. To express the phase error in terms of X and Y, define $\Omega \equiv \sqrt{(X^2+Y^2+Z^2)}$. For sufficiently small regions in Fourier space, write $Z = aX + bY + c$, and also define a functional relationship between the lateral viewing angle and the range: $R_n = g(tan\theta_n)$. Then (14) becomes

$$\phi_e(X,Y) = z_o Z + \frac{\Omega}{2g(\frac{-Y}{X})} \cdot [x_o^2 + y_o^2 + z_o^2 - (x_o\frac{X}{\Omega} + y_o\frac{Y}{\Omega} + z_o\frac{Z}{\Omega})^2]. \quad (16)$$

Here, the partial derivatives of $g(\cdot)$ are

$$\frac{\partial g}{\partial X} = \frac{dg}{dt}\cdot\frac{dt}{d(tan\theta)}\cdot\frac{\partial(-Y/X)}{\partial X} = \frac{\dot{R}}{\dot{\theta}}cos^2\theta\frac{Y}{X^2}, \quad (17)$$

$$\frac{\partial g}{\partial Y} = \frac{\dot{R}}{\dot{\theta}}cos^2\theta\frac{-1}{X} \quad (18)$$

where $\theta \equiv tan^{-1}(-Y/X)$, and $R \equiv g(-Y/X)$. No imaging is possible for $\dot{\theta} = 0$. Then the amount of shift is

$$\Delta x_o = \frac{\partial\phi_e}{\partial X}|_{(X_o,Y_o)} = az_o + \frac{r_o^{\perp}(x_o,y_o,z_o)^2}{2R_o}(\frac{\partial\Omega}{\partial X}|_o + \frac{\dot{R}_o}{R_o\dot{\theta}_o}\frac{sin\theta_o}{cos\psi_o}) + \frac{r_o^R(x_o,y_o,z_o)^2}{R_o}(\frac{\partial\Omega}{\partial X}|_o - \frac{x_o+az_o}{r_o^R(x_o,y_o,z_o)}) \quad (19)$$

$$\Delta y_o = \frac{\partial\phi_e}{\partial Y}|_{(X_o,Y_o)} = bz_o + \frac{r_o^{\perp}(x_o,y_o,z_o)^2}{2R_o}(\frac{\partial\Omega}{\partial Y}|_o + \frac{\dot{R}_o}{R_o\dot{\theta}_o}\frac{cos\theta_o}{cos\psi_o}) + \frac{r_o^R(x_o,y_o,z_o)^2}{R_o}(\frac{\partial\Omega}{\partial Y}|_o - \frac{y_o+bz_o}{r_o^R(x_o,y_o,z_o)}) \quad (20)$$

where

$$\frac{\partial\Omega}{\partial X}|_o = \frac{X_o+aZ_o}{\Omega_o} = cos\theta_o cos\psi_o - asin\psi_o$$
$$\frac{\partial\Omega}{\partial Y}|_o = \frac{Y_o+bZ_o}{\Omega_o} = -sin\theta_o cos\psi_o - bsin\psi_o. \quad (21)$$

The subscript naught is used to indicate values evaluated at (X_o, Y_o), e.g. $R_o = g(-Y_o/X_o)$, $\theta_o = tan^{-1}(-Y_o/X_o)$, etc. In (19) and (20), the terms involving a or b are due to vertical variation in the radar path, and the terms involving R_o are due to the curvature of the wavefront. Usually the latter will be small for large R_o in the denominator. However, when the ratio of $\dot{R}$ to $R\dot{\theta}$ is large, then wavefront curvature may cause a perceptible shift, as is the case for severely squinted SAR [5]. A high ratio indicates that the radial velocity component is much larger than the lateral component, as would be true in runway imaging for an aircraft landing application. If the range changes rapidly enough during data collection, the *change* in the curvature of the wavefront leads to phase errors that are more significant than that caused by the curvature alone.

4. IMAGE RECONSTRUCTION

For an arbitrary radar path, we can partition the corrupted Fourier data into subsets with approximately linear phase error, and process each subset separately using an inverse FFT, after interpolating the samples to a Cartesian grid. In general, suppose we wish to form a 2-D image

$$\hat{f}(x,y) = f(x,y,z_o(x,y)), \quad (22)$$

where $z_o(\cdot,\cdot)$ is a function describing the surface. Since a general reflectivity function can be modeled as the superposition of several point scatterers, first consider imaging the single point scatterer in (6). If we process a rectangular segment of corrupted Fourier data with an inverse two-dimensional FFT, the resulting subimage will be

$$g(x,y) = \frac{1}{(2\pi)^2}\int_{-\pi}^{\pi}dX\int_{-\pi}^{\pi}dY\hat{F}(X,Y)\cdot e^{-j\phi_e(X,Y)}\cdot e^{j(xX+yY)} = \frac{e^{-j\zeta}}{(2\pi)^2}\int_{-\pi}^{\pi}dX\int_{-\pi}^{\pi}dY\cdot e^{-j[(x_o+\Delta x_o-x)X+(y_o+\Delta y_o-y)Y]}, \quad (23)$$

where X and Y have been normalized to vary over $[-\pi,\pi]$, and

$$\zeta(x_o,y_o) \equiv \phi_e(X_o,Y_o) - \Delta x_o X_o - \Delta y_o Y_o. \quad (24)$$

Then

$$g(x,y) = e^{-j\zeta}sinc(x-x_o-\Delta x_o)sinc(y-y_o-\Delta y_o). \quad (25)$$

The point-scatterer location will be shifted according to (19) and (20). For a more general reflectivity function, where

$$\hat{f}(x,y) = \sum_k \sigma_k\delta(x-x_k, y-y_k), \quad (26)$$

the corresponding subimage would be

$$g(x,y) = \sum_k \sigma_k e^{-j\zeta(x_k,y_k)}\cdot sinc(x-x_k-\Delta x_k)\cdot sinc(y-y_k-\Delta y_k). \quad (27)$$

Each subimage is "warped" differently, depending on the values $R_o, \dot{R}_o, \theta_o, \dot{\theta}_o$, and ψ_o that correspond to the center of that Fourier data subset, and the appropriate a, b, c.

If the function $z_o(x,y)$ is known, it is possible to reverse the warping to some degree, and use the corrected subimages to form a single higher-resolution image. The subimages can be unwarped according to

$$\tilde{f}(x,y) = g(x+\Delta x, y+\Delta y)e^{j\zeta(x,y)}, \quad (28)$$

since a point scatterer at (x,y) appears at $(x+\Delta x, y+\Delta y)$ in the warped image g. This shifts the *peak* of each sinc component by the correct amount.

For a simple demonstration, consider a 1-D scattering surface with two point scatterers along the y-axis, and a "rooftop-shaped" radar path where z_n increases linearly for half of the data samples, and then decreases at the same

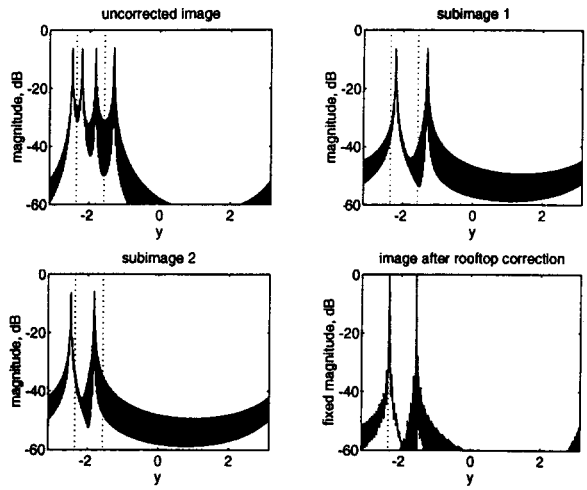

Figure 2: A high-quality high-resolution image is formed by unwarping the low-resolution subimages.

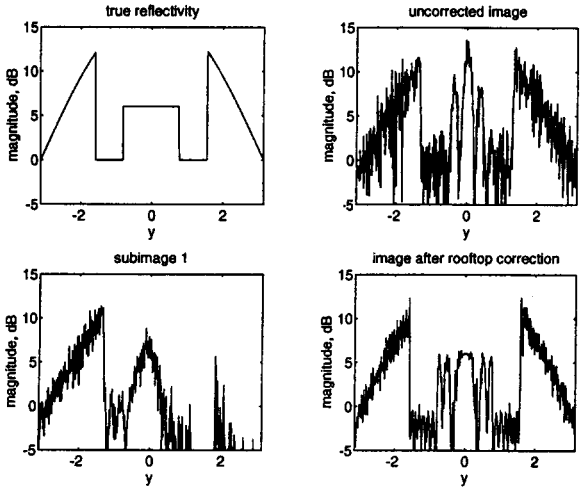

Figure 3: A high-resolution image of an extended target exhibits speckle for complex reflectivity with random phase.

rate for the other half. Assume $\dot{R} \approx 0$ and R large so that $\Delta x_o \approx a z_o$ and $\Delta y_o \approx b z_o$. Suppose that corrupted Fourier data samples are known for $X = \frac{2\omega_o}{c}$, $|Y| \leq \pi$, with $Z = C(\pi - |Y|)$. Let $z_o(x,y) = Bcos(y/2)$ for $|y| \leq \pi$. If the Fourier data are processed with a 1-D inverse FFT, the resulting image would be Figure 2a. The point scatterers should appear where the vertical dotted lines appear, but for $C = 3$ and $B = 10$ the resulting image is degraded. This image is the superposition of two subimages (2b and 2c) that correspond to the two segments of the rooftop (two subsets of Fourier data). So that the subimages will contain the same number of points, each subimage was formed by zeroing the Fourier samples belonging to the other subset, and computing an inverse FFT. The spatially-varying shift is apparent here. If the subimages are corrected according to (28) and then added together, the point scatterers appear sharply in their correct positions (see Figure 2d).

Now consider imaging an extended target with the same scenario as before, but with reflectivity magnitude as shown in Figure 3a. This extended target is actually composed of a cluster of point scatterers on the y-axis, with reflectivity phase randomly varied [6] between 0 and 2π. The phase of the reflectivity, though randomly selected, is assumed to remain constant for various viewing positions. Figure 3b shows the corresponding uncorrected image. One subimage is shown in Figure 3c; the other subimage is similar, but flipped. Note that only some of the scatterers are observable in each subimage. After correction according to (28), the two subimages are added to get the image in Figure 3d. The measured data do not generally specify a unique solution, but in assuming that unknown Fourier samples are zero, we implicitly obtain minimum-norm solutions for the subimages, hence, the extra nulls in the image. The noisy appearance is analogous to speckle in a 2-D image.

5. SUMMARY

Given radar data collected along an arbitrary data path, we have demonstrated that it is possible to construct 2-D images of 3-D surfaces if the elevation function of the surface, $z_o(x,y)$, is known. By partitioning the data into subsets that can be interpreted as Fourier data with a linear phase error, and deriving the corresponding shifts and phase distortion, we are able to compensate for the distortion in the corresponding subimages. The subimages can be formed efficiently using the usual FFT processing, before compensating for the distortion, and combining the images to form a high-resolution image. The compensation is not exact, since it shifts only the *peaks* of sinc components by the correct amount, but the processing is well conditioned, and it produces improved results.

6. REFERENCES

[1] J.L.H. Webb, D.C. Munson, Jr., and N.J.S. Stacy, "High-resolution planetary imaging via spotlight-mode synthetic aperture radar", in *Proc. IEEE International Conference on Image Processing*, Austin, TX, November 13-16, 1994, vol. I, pp. 451–455.

[2] J.L. Walker, "Range-Doppler imaging of rotating objects", *IEEE Trans. Aerospace and Electronic Systems*, vol. AES-16, pp. 23–52, January 1980.

[3] C.V.Jakowatz, Jr. and P.A.Thompson, "The tomographic formulation of spotlight mode synthetic aperture radar extended to three dimensional targets", in *Proc. 1992 Digital Signal Proc. Workshop*, Starved Rock State Park, Utica, IL, Sept. 13-16, 1992, pp. 5.6.1–2.

[4] M.R. Coble and D.C. Munson, Jr., "Inverse SAR planetary imaging", in *Proc. International Conference on Image Processing: Theory and Applications*, San Remo, Italy, June 14-16, 1993.

[5] Jung Ah Lee and D.C. Munson, Jr., "Effect of a nonplanar wavefront in spotlight-mode synthetic aperture radar", in *Proc. IEEE International Conference on Image Processing*, Austin, TX, Nov. 13-16, 1994, vol. I, pp. 481–485.

[6] D.C. Munson, Jr. and J.L.C.Sanz, "Image reconstruction from frequency-offset Fourier data", *Proceedings of the IEEE*, pp. 661–669, June 1984.